Modeling and Motion Stability Analysis of Skid-Steered Mobile Robots

Hongpeng Wang, Junjie Zhang, Jingang Yi, Dezhen Song, Suhada Jayasuriya, and Jingtai Liu

***Abstract*— Skid-steered mobile robots are widely used because of the simplicity of mechanism and high reliability. However, understanding of the kinematics and dynamics of such a robotic platform is challenging due to the complex wheel/ground interactions and kinematic constraints. In this paper, we attempt to develop a kinematic and dynamic modeling scheme to analyze the skid-steered mobile robot. We model wheel/ground interaction and analyze the robot motion stability. As an application example, we present how to utilize the kinematic and dynamic modeling and analysis for robot localization and slip estimation using only low-cost strapdown inertial measurement units (IMU). The extended Kalman filter (EKF)-based localization scheme incorporates the kinematic constraints. The performance of the EKF-based localization and slip estimation scheme are presented. The estimation methodology is tested and validated on a robotic testbed.**

I. Introduction

Skid-steering is a widely used locomotion mechanism for mobile robots. For a skid-steered robot (Fig. 1), there is no steering mechanism and motion direction is changed by turning the left- and right-side wheels at different velocities. Due to complex wheel/ground interactions and kinematic constraints, it remains a challenging task to obtain an accurate kinematic and dynamic model for skid-steered robots.

The focus of this paper is on understanding of the kinematics and dynamics of skid-steered mobile robots, and its applications to robot localization. The results presented in this paper are the extension of our previous work in [1], [2]. In [1], we reveal underlying geometric and kinematic relationships between wheel slips and instantaneous rotation centers of the left- and right-side wheels and the robot platform of a four-wheel skid-steered robot (Fig. 1). An inertial measurement units (IMU)-based localization scheme is also presented in [1]. In [2], we present a linearized traction/braking forces model. In this paper, we further extend the robot dynamics modeling and provide motion stability conditions. We also analyze the stability and convergence performance of the IMU-based localization scheme. The new analysis and development are experimentally tested and validated.

This work is supported in part by the National Science Foundation under grant CMMI-0856095 (J. Yi) and a fellowship from China Scholarship Council (H. Wang).

H. Wang and J. Liu are with the Institute of Robotics and Automation Information Systems, Nankai University, Tianjing 300071, P.R. China. Email: wanghp@robot.nankai.edu.cn (H. Wang) and liujt@robot.nankai.edu.cn (J. Liu).

J. Zhang and S. Jayasuriya are with the Department of Mechanical Engineering, Texas A&M University, College Station, TX 77843 USA. Email: jjzhang@tamu.edu (J. Zhang) and sjayasuriya@tamu.edu (S. Jayasuriya).

J. Yi is with the Department of Mechanical and Aerospace Engineering, Rutgers University, Piscataway, NJ 08854 USA. Email: jgyi@rutgers.edu.

D. Song is with the Department of Computer Science, Texas A&M University, College Station, TX 77843 USA. Email: dzsong@cs.tamu.edu.

The contributions of this study are two-folds. First, the proposed kinematic modeling and analysis of the skid-steered robot provide a new framework to study this type of robotic platform. As a direct application, we discuss the convergence and performance of the extended Kalman filter (EKF)-based localization scheme. Second, using a wheel/ground interaction model, we analyze the robot motion and provide a new framework to analyze the skid motion stability conditions. The dynamic modeling and analysis can be further used for robot motion planning and control.

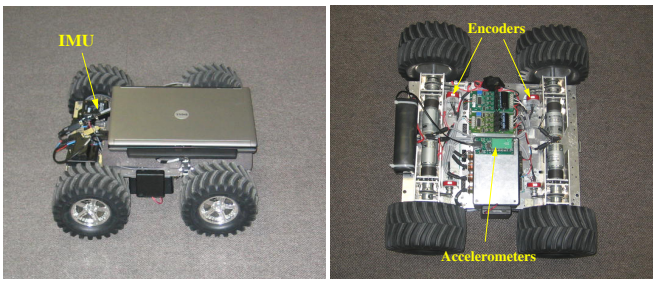

(a) (b)

Fig. 1. A skid-steered four-wheel mobile robot with a sensor suite.

The remainder of this paper is organized as follows. We start reviewing some related work in Section II. In Section III, we discuss the kinematics-based localization scheme. We then discuss the dynamic modeling and skid motion stability in Section IV. Experimental results are presented in Section V before we conclude the paper.

II. Related Work

Dynamic modeling and control of differential-driven mobile robots, such as unicycle or car-like robots, have been extensively studied in the past two decades. The nonholonomic constraint of zero lateral velocity of wheel contact point is normally considered for differential-driven mobile robots. For skid-steered mobile robots, non-zero wheel lateral velocity is allowed, and the zero-velocity constraint is no longer valid.

Methods of modeling tracked vehicles have been utilized for modeling skid-steered mobile robots [3], [4]. In [5], an extra wheeled trailer is designed to experimentally study the kinematic relationship for simultaneous localization and mapping (SLAM) applications. It is concluded that a kinematic model for an ideal differential-driven wheeled robot cannot be used for skid-steered robots. In [6], geometric analogy with an ideal differential-driven wheeled mobile robot is studied and experimental validations have been carried out for skid-steered mobile robots. In [7], stability studies of the skid-steered robot have been discussed. It is

concluded that the position of the rotation center of the robot has been located within the wheel base for a stable motion.

Wheel slip plays a critical role in kinematic and dynamic modeling of skid-steered mobile robots. The slip is typically defined as a non-dimensional relative motion of the wheel contact patch to the ground. Wheel slip information is important for robot localization applications [8]. The wheel slip also plays an important role in robot dynamics and control. The pseudo-static relationship between the friction coefficient and the wheel slip is observed in automotive tire/road interaction. A linearized approximation of the pseudo-static friction model is proposed to capture friction forces by one unified formulation [2]. One of advantages of such a modeling approach is to relate the friction forces to kinematic variables, such as wheel rotation velocities. We extend the dynamic modeling in [2] to study the robot motion stability.

The accuracy of the dead-reckoning localization deteriorates when there is a large wheel slip. In [9], the error reduction of the odometry of the skid-steered robots is discussed for dead-reckoning applications using encoder and motor current measurement information. In [6], [10], the localization of a tracked vehicle is presented based on kinematic models. In [11], an IMU-based wheel slip detection scheme is designed for a car-like mobile robot using a dynamic model-based EKF design. In [8], wheel slip is compensated in an EKF-based localization design. In [12], velocity constraints, such as zero lateral velocity, are integrated with an EKF to enhance the localization of an autonomous ground vehicle. Wheel slip is however not considered in the EKF design in [12]. In this paper, we extend the developed robot models and enhance the localization scheme for the skid-steered robots in [1]. We also analyze the performance of the localization scheme.

III. Robot Kinematics-Based Localization

A. Kinematic modeling

Fig. 2 shows the kinematics schematic of the skid-steered robot. Similar to [1], we consider that each side's two wheels rotate at the same speed and that all four wheels run at the same velocity directions. We also assume that the robot is running on a firm ground surface, and four wheels always contact the ground surface.

Let ω_i and v_i, $i = 1, \cdots, 4$, denote the wheel angular and center linear velocities for front-left, rear-left, front-right, and rear-right wheels, respectively. From the above assumption, we have $\omega_L := \omega_1 = \omega_2$ and $\omega_R := \omega_3 = \omega_4$. We define an inertial frame $\mathcal{I}\,(X, Y, Z)$ and a robot body frame $\mathcal{B}\,(x, y, z)$ as shown in Fig. 2. We use Euler angles to describe the transformation between frames $\mathcal{B}$ and $\mathcal{I}$. Let $\mathbf{\Theta} := [\phi \;\; \theta \;\; \psi]^T$ denote the attitude angles, namely, the roll angle ϕ, pitch angle θ, and yaw angle ψ, respectively. The transformation from $\mathcal{I}$ to $\mathcal{B}$ is considered as the Z-Y-X ordered Euler angle rotation by the following matrix

$$C_B^I = \begin{bmatrix} c_\theta c_\psi & -s_\psi c_\phi + c_\psi s_\phi s_\theta & s_\phi s_\psi + c_\psi s_\theta c_\phi \\ c_\theta s_\psi & c_\phi c_\psi + s_\theta s_\phi s_\psi & -s_\phi c_\psi + s_\theta c_\phi s_\psi \\ -s_\theta & c_\theta s_\phi & c_\phi c_\theta \end{bmatrix}, \tag{1}$$

where $c_\theta := \cos\theta$, $s_\theta := \sin\theta$, and the same notation for the angles ϕ and ψ.

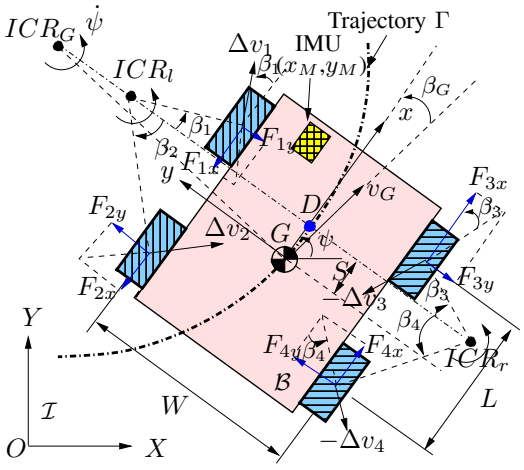

Fig. 2. A top-view schematic of a skid-steered mobile robot.

Let L and W denote the longitudinal and lateral wheel bases, respectively. Let $(x_M, y_M, 0)$ denote the IMU location in $\mathcal{B}$. We define the longitudinal wheel slip λ_i at each wheel

$$\lambda_i := \frac{r\omega_i - v_{ix}}{r\omega_i}, \quad i = 1, \ldots, 4, \tag{2}$$

where r is the effective wheel radius. Let ICR_l, ICR_r, and ICR_G denote the instantaneous center of rotation (ICR) of the left-side wheel contact points, right-side wheel contact points, and the robot body, respectively. We denote the coordinates for ICR_l, ICR_r, and ICR_G in $\mathcal{B}$ as $(x_{lc}, y_{lc}, 0)$, $(x_{rc}, y_{rc}, 0)$, and $(x_{Gc}, y_{Gc}, 0)$, respectively. It is known that ICR_l, ICR_r and ICR_G lie on a line parallel to the y-axis [1]. We define the *longitudinal ICR location*, denoted as S, as the x-coordinate of the collinear ICR_l, ICR_r, and ICR_G in $\mathcal{B}$. Then, S satisfies the following constraints [6], [13], [14].

$$S = x_{lc} = x_{rc} = x_{Gc} = -\frac{v_{Gy}}{\dot{\psi}}. \tag{3}$$

Let $\mathbf{P}_I(t) = [X_I(t) \;\; Y_I(t) \;\; Z_I(t)]^T \in \mathbb{R}^3$ and $\mathbf{V}_I(t) = [V_x(t) \;\; V_y(t) \;\; V_z(t)]^T \in \mathbb{R}^3$ denote the position and velocity vectors of the IMU in $\mathcal{I}$, respectively. We denote the IMU acceleration and angular rate measurements as $\mathbf{A}_B = [a_{Bx} \;\; a_{By} \;\; a_{Bz}]^T$ and $\boldsymbol{\omega}_B = [\omega_{Bx} \;\; \omega_{By} \;\; \omega_{Bz}]^T$, respectively. We obtain the following motion equations [12].

$$\dot{\mathbf{P}}_I = \mathbf{V}_I, \tag{4a}$$
$$\dot{\mathbf{V}}_I = C_B^I \mathbf{A}_B + \mathbf{G}, \tag{4b}$$
$$\dot{\phi} = \omega_{Bx} + s_\phi \tan\theta \omega_{By} + c_\phi \tan\theta \omega_{Bz}, \tag{4c}$$
$$\dot{\theta} = c_\phi \omega_{By} - s_\phi \omega_{Bz}, \tag{4d}$$
$$\dot{\psi} = \frac{s_\phi}{c_\theta}\omega_{By} + \frac{c_\phi}{c_\theta}\omega_{Bz}, \tag{4e}$$

where $\mathbf{G} = [0 \;\; 0 \;\; -g]^T$ and g is the gravitational constant.

We consider the robot velocity estimates and constraints in the body frame $\mathcal{B}$. It is straightforward to obtain the following velocity constraint in the z-axis direction.

$$v_{Bz} = 0. \tag{5}$$

For the IMU longitudinal velocity v_{Bx}, we obtain

$$v_{Bx} = \frac{r}{2}\left[(\omega_L + \omega_R) - (\lambda'_L\omega_L + \lambda'_R\omega_R)\right] + x_M\dot{\psi}, \quad (6)$$

where

$$\lambda'_L(\lambda'_R) = \begin{cases} \max\{\lambda_L(\lambda_R), 0\} & \text{if } \omega_L \geq \omega_R \ (\omega_L \leq \omega_R) \\ \min\{\lambda_L(\lambda_R), 0\} & \text{if } \omega_L < \omega_R \ (\omega_L > \omega_R). \end{cases} \quad (7)$$

For the lateral velocity v_{By}, we obtain

$$v_{By} = (S + x_M)\dot{\psi}. \quad (8)$$

We have to estimate the value of S. In [1], we introduce a non-dimensional variable γ as

$$\gamma := \frac{(1-\lambda_L) - (1-\lambda_R)\kappa_\omega}{(1-\lambda_L) + (1-\lambda_R)\kappa_\omega}, \quad (9)$$

where $\kappa_\omega = \frac{\omega_R}{\omega_L}$. The value of S is considered as a function of variable γ. We approximate the function S in (8) by $\hat{S}$ as

$$\hat{S} := \hat{S}(\gamma) = \frac{a_1}{a_2|\gamma| + a_3}, \quad (10)$$

where the coefficients $a_1 = 2.148$ cm, $a_2 = 0.249$, and $a_3 = 0.039$ are obtained by data-fitting the experimental data [1]. We also define the S estimation error $e_S(t) := S - \hat{S}$. Since $\omega_L > 0$, $\omega_R > 0$ and wheel slip $|\lambda| \leq 1$, it is straightforward to obtain that $-1 \leq \gamma \leq 1$.

B. EKF design

The IMU velocities in $\mathcal{B}$ are considered as the measurements $\mathbf{y}(t) \in \mathbb{R}^3$, namely,

$$\mathbf{y}(t) = \mathbf{h}(\mathbf{v}_B) := \begin{bmatrix} v_{Bx} \\ v_{By} \\ v_{Bz} \end{bmatrix} = (C_B^I)^T\mathbf{V}_I. \quad (11)$$

Considering the wheel encoder measurement noise and ground topography, we modify (11) and re-write in discrete-time form as

$$\mathbf{y}(k) = \mathbf{h}(\mathbf{v}_B(k)) + \mathbf{w}(k). \quad (12)$$

We define the state variable $\mathbf{X}(t) := [\mathbf{P}_I^T(t)\ \mathbf{V}_I^T(t)\ \mathbf{\Theta}^T(t)]^T \in \mathbb{R}^9$ and re-write the kinematics (4) in a discrete-time form as

$$\mathbf{X}(k) = \mathbf{X}(k-1) + \Delta T\mathbf{f}\left(\mathbf{X}(k-1), \mathbf{u}(k-1)\right), \quad (13)$$

where $\mathbf{u}(k) := [\mathbf{A}_B^T(k)\ \ \boldsymbol{\omega}_B^T(k)]^T$ is the IMU measurements at the kth sampling time, $k \in \mathbb{N}$, and ΔT is the data-sampling period. The function $\mathbf{f}\left(\mathbf{X}(k), \mathbf{u}(k)\right)$ is given in (4) as

$$\mathbf{f}\left(\mathbf{X}(k), \mathbf{u}(k)\right) = \begin{bmatrix} \mathbf{f}_P \\ \mathbf{f}_V \\ \mathbf{f}_\Theta \end{bmatrix} := \begin{bmatrix} \mathbf{V}_I(k) \\ C_B^I(k)\mathbf{A}_B^T(k) + \mathbf{G} \\ \mathbf{f}_\Theta(\mathbf{\Theta}(k), \boldsymbol{\omega}_B(k)) \end{bmatrix}, \quad (14)$$

where $\mathbf{f}_P = \mathbf{V}_I(k)$, $\mathbf{f}_V = C_B^I\mathbf{A}_B^T(k) + \mathbf{G}$, and

$$\mathbf{f}_\Theta(\mathbf{\Theta}(k), \boldsymbol{\omega}_B(k)) := \begin{bmatrix} \omega_{Bx} + \tan\theta\left(s_\phi\omega_{By} + c_\phi\omega_{Bz}\right) \\ c_\phi\omega_{By} - s_\phi\omega_{Bz} \\ \frac{s_\phi}{c_\theta}\omega_{By} + \frac{c_\phi}{c_\theta}\omega_{Bz} \end{bmatrix}.$$

An EKF design is applied to the system (13) and (11). For (13), we obtain the Jacobian matrix $\mathbf{F}(k)$ as

$$\mathbf{F}(k) = \begin{bmatrix} \mathbf{I}_3 & \Delta T\mathbf{I}_3 & \mathbf{0}_3 \\ \mathbf{0}_3 & \mathbf{I}_3 & \Delta T\mathbf{F}_V(k) \\ \mathbf{0}_3 & \mathbf{0}_3 & \mathbf{I}_3 + \Delta T\mathbf{F}_\Theta(k) \end{bmatrix}, \quad (15)$$

where $\mathbf{I}_n$ and $\mathbf{0}_n$, are the $n \times n$ identity and zero matrices, respectively, $\mathbf{F}_\Theta := \frac{\partial \mathbf{f}_\Theta}{\partial \mathbf{\Theta}}$, and $\mathbf{F}_V := \frac{\partial \mathbf{f}_V}{\partial \mathbf{\Theta}}$. The Jacobian matrix $\mathbf{H}(k)$ for (11) is calculated as

$$\mathbf{H}(k) = \frac{\partial \mathbf{h}}{\partial \mathbf{X}}\Big|_{\mathbf{X}(k)} = \begin{bmatrix} \mathbf{0}_3 & \mathbf{H}_V(k) & \mathbf{H}_\Theta(k) \end{bmatrix}, \quad (16)$$

where $\mathbf{H}_V(k) := \frac{\partial \mathbf{h}(\mathbf{v}_B)}{\partial \mathbf{V}_I} = (C_B^I(k))^T$ and $\mathbf{H}_\Theta := \frac{\partial \mathbf{h}(\mathbf{v}_B)}{\partial \mathbf{\Theta}}$.

The EKF can be written as a prediction step ($\hat{\mathbf{X}}(k|k-1)$) and a correction step ($\hat{\mathbf{X}}(k|k)$) recursively. The convergence of the EKF design is directly related to the robot motion of the robot. We use the longitudinal velocity calculation in (6) by constraining the slip range in (7). For a clarity of analysis purposes, we neglect the noise models in the EKF design to focus on how to utilize the robot modeling and analysis information for localization estimation. We have implemented IMU noise models in [11] in experiments.

C. Velocity estimation error analysis

In this subsection, we analyze the velocity estimation error under the condition of a bounded attitude estimation. Let $\hat{\mathbf{V}}_I$ denote the estimated velocity under the estimated attitude $\hat{\mathbf{\Theta}}$. From (4b), we obtain $\dot{\hat{\mathbf{V}}}_I = \hat{C}_B^I\mathbf{A}_B + \mathbf{G}$, where $\hat{C}_B^I := C_B^I(\hat{\mathbf{\Theta}})$. The estimated errors for velocity and attitude are defined as $\mathbf{e}_V := \mathbf{V}_I - \hat{\mathbf{V}}_I$ and $\mathbf{e}_\Theta := \mathbf{\Theta} - \hat{\mathbf{\Theta}} = [\Delta\phi\ \ \Delta\theta\ \ \Delta\psi]^T$, respectively. Here, $\Delta\phi := \phi - \hat{\phi}$, $\Delta\theta := \theta - \hat{\theta}$, and $\Delta\psi := \psi - \hat{\psi}$ are the estimation errors for roll, pitch, and yaw angles, respectively. We assume the estimated attitude error $\mathbf{e}_\Theta$ is bounded.

From (4b), we obtain the error dynamics

$$\dot{\mathbf{e}}_V = \Delta C_B^I\mathbf{A}_B, \quad (17)$$

where $\Delta C_B^I := C_B^I - \hat{C}_B^I$. Using Taylor expansion, we approximate ΔC_B^I as

$$\Delta C_B^I = -\left(\frac{\partial C_B^I}{\partial\phi}\Delta\phi + \frac{\partial C_B^I}{\partial\theta}\Delta\theta + \frac{\partial C_B^I}{\partial\psi}\Delta\psi\right), \quad (18)$$

and (17) is then re-written as

$$\dot{\mathbf{e}}_V = -\mathbf{F}_V\mathbf{e}_\Theta. \quad (19)$$

The above estimation error analysis only considers the kinematic relationship (4b) under attitude estimation errors. We have to incorporate the above analysis with the EKF correction step. Since the EKF design is implemented in a discrete-time form, we also analyze the velocity estimation errors in the discrete-time form for presentation convenience. We rewrite error definitions in the discrete-time form as $\mathbf{e}_V(k|k-1) := \mathbf{V}_I(k) - \hat{\mathbf{V}}_I(k|k-1)$, $\mathbf{e}_\Theta(k|k-1) := \mathbf{\Theta}(k) - \hat{\mathbf{\Theta}}(k|k-1)$, and define the EKF velocity estimation error $\mathbf{e}_V(k|k) := \mathbf{V}_I(k) - \hat{\mathbf{V}}_I(k|k)$. Error dynamics (19) is re-written in discrete-time form as

$$\mathbf{e}_V(k|k-1) = \mathbf{e}_V(k-1|k-2) - \Delta T\mathbf{F}_V(k)\mathbf{e}_\Theta(k|k-1). \quad (20)$$

and $\mathbf{e}_V(k|k) = \mathbf{e}_V(k|k-1) - \left(\tilde{\mathbf{X}}(k)\right)_{4:6}$, where $\tilde{\mathbf{V}}_I(k) := \hat{\mathbf{V}}_I(k|k) - \hat{\mathbf{V}}_I(k|k-1)$, $\tilde{\mathbf{X}}(k) := \hat{\mathbf{X}}(k|k) - \hat{\mathbf{X}}(k|k-1)$, and operator $(\mathbf{X})_{i:j}$, $i \geq j$, forms a column vector by taking the ith to jth elements from the column vector $\mathbf{X}$. We denote the EKF correction gain matrix $\mathbf{W}(k) := [\mathbf{W}_1^T(k) \quad \mathbf{W}_2^T(k) \quad \mathbf{W}_3^T(k)]^T \in \mathbb{R}^{9\times 3}$, where $\mathbf{W}_i(k) \in \mathbb{R}^{3\times 3}$, $i = 1, 2, 3$. From EKF design and (16), we have

$$\begin{aligned}\tilde{\mathbf{V}}_I(k) &= \left(\mathbf{W}(k)\left[\mathbf{y}(k) - \mathbf{H}(k)\hat{\mathbf{X}}(k|k-1)\right]\right)_{4:6} \\ &= \mathbf{W}_2(k)\left[\mathbf{H}_V(k)\mathbf{e}_V(k|k-1) + \mathbf{H}_\Theta(k)\mathbf{e}_\Theta(k|k-1)\right] \\ &\quad -\mathbf{W}_2(k)\left[\mathbf{y}(k) - \mathbf{H}(k)\mathbf{X}(k)\right]. \end{aligned} \tag{21}$$

We neglect the second part of the calculation (21) for the first-order approximation of the output $\mathbf{y}(k)$. Using (21), we obtain

$$\begin{aligned}\mathbf{e}_V(k|k) = &\left[\mathbf{I}_3 - \mathbf{W}_2(k)\mathbf{H}_V(k)\right]\mathbf{e}_V(k|k-1) \\ &-\mathbf{W}_2(k)\mathbf{H}_\Theta(k)\mathbf{e}_\Theta(k|k-1). \end{aligned} \tag{22}$$

In our examples, the mobile robot is running on flat horizontal ground surfaces, and we approximate $\phi = \theta = 0$. Therefore, using (20) and neglecting the attitude dynamics, the velocity estimation errors $\mathbf{e}_v(k|k-1) := \left(C_B^I(k)\right)^T \mathbf{e}_V(k|k-1)$ in $\mathcal{B}$ satisfy the following dynamic equations

$$\begin{aligned}\mathbf{e}_v(k|k-1) = &\,\mathbf{e}_v(k-1|k-2) - \\ &\Delta T\left(C_{B0}^I(k)\right)^T \mathbf{F}_V(k)\mathbf{e}_\Theta(k|k-1) \end{aligned} \tag{23}$$

where

$$C_{B0}^I(k) := C_B^I(0, 0, \psi(k)) = \begin{bmatrix} c_{\psi(k)} & -s_{\psi(k)} & 0 \\ s_{\psi(k)} & c_{\psi(k)} & 0 \\ 0 & 0 & 1 \end{bmatrix}$$

Similarly, the EKF velocity estimation errors (22) reduce to

$$\begin{aligned}\mathbf{e}_v(k|k) = &\left[\mathbf{I}_3 - \left(C_{B0}^I(k)\right)^T \mathbf{W}_2(k)\right]\mathbf{e}_v(k|k-1) \\ &-\left(C_{B0}^I(k)\right)^T \mathbf{W}_2(k)\begin{bmatrix} v_{By}(k) \\ -v_{Bx}(k) \\ 0 \end{bmatrix}\Delta\psi(k) \end{aligned} \tag{24}$$

Therefore, from (23) and (24), the estimation velocity $\mathbf{e}_v(k|k)$ can grow even if the attitude estimation error, such as $\Delta\psi(k)$, is bounded.

IV. Skid Motion Stability

A. Robot dynamics

We consider the dynamics equations of skid-steered mobile robots under a planar motion and derive the skidding motion stability conditions. Let F_{ix} and F_{iy} denote the longitudinal and the lateral forces at the ith wheel, respectively; see Fig. 2. We consider the longitudinal friction forces $F_{ix} = N_i\mu_i$, where μ_i is the friction coefficient and N_i is the normal force. It has been widely accepted that the friction coefficient μ is a function of the wheel slip λ. We here consider a linear approximation of the μ-λ curve as shown in Fig. 3. Let λ_m denote the slip value that corresponds to the maximum friction coefficient. When slip $\lambda \leq \lambda_m$, the wheel runs in a stable region while $\lambda > \lambda_m$, the wheel runs in a unstable region. An important feature of the linear approximation is the preservation of the two-region characteristic.

The friction coefficient μ can be written by the following functions [2].

$$\mu(\lambda) = K\left[\sigma_1(\lambda) + \sigma_2(\lambda)\,\mathrm{sgn}(\lambda)\lambda\right], \tag{25}$$

where K is the wheel stiffness coefficient, $\mathrm{sgn}(x) = 1$ if $x \geq 0$ and $\mathrm{sgn}(x) = -1$ if $x < 0$, $\sigma_1(\lambda) = 0$, if $0 \leq \lambda < \lambda_m$; and $\frac{1-\alpha\lambda_m}{1-\lambda_m}\lambda_m$, if $\lambda \geq \lambda_m$, $0 \leq \alpha \leq 1$, and $\sigma_2(\lambda) = 1$, if $0 \leq \lambda < \lambda_m$; and $-\frac{1-\alpha}{1-\lambda_m}\lambda_m$, if $\lambda \geq \lambda_m$.

Using the geometric relationship [2], we write the dynamic equations of the robot center G in $\mathcal{B}$ as follows.

$$\dot{v}_{Gx} = gK\left[\frac{1}{2}\sigma_\Sigma + \frac{1}{4}W\dot{\psi}v_1 - \frac{1}{2}v_{Gx}v_2\right], \tag{26a}$$

$$\dot{v}_{Gy} = -\frac{1}{2}gKv_{Gy}\left[v_2\left(1 + \frac{1}{2}\sigma_{r1}\right) + \frac{1}{2}\sigma_{r2}v_1\right], \tag{26b}$$

$$\begin{aligned}\ddot{\psi} = \frac{mg}{4I_G}K\Bigg\{&-W\sigma_\Delta + \left(Wv_{Gx} + \frac{L^2}{2}\dot{\psi}\sigma_{r1}\right)v_1 - \\ &\frac{1}{2}\left[W^2 + L^2\left(1 + \frac{1}{2}\sigma_{r2}\right)\right]\dot{\psi}v_2\Bigg\}, \end{aligned} \tag{26c}$$

where m is the mass of the robot, I_G is the mass moment of inertia of the robot about G, $\sigma_{r1} = \frac{\sigma_1(\lambda_1)\,\mathrm{sgn}(\lambda_1\dot{\psi})}{\lambda_1\sigma_2(\lambda_1)} - \frac{\sigma_1(\lambda_3)\,\mathrm{sgn}(\lambda_3\dot{\psi})}{\lambda_3\sigma_2(\lambda_3)}$, $\sigma_{r2} = \frac{\sigma_1(\lambda_1)\,\mathrm{sgn}(\lambda_1\dot{\psi})}{\lambda_1\sigma_2(\lambda_1)} + \frac{\sigma_1(\lambda_3)\,\mathrm{sgn}(\lambda_3\dot{\psi})}{\lambda_3\sigma_2(\lambda_3)}$, and $\sigma_\Sigma = \sigma_{1\Sigma} + \sigma_{2\Sigma}$, $\sigma_\Delta = \sigma_{1\Delta} + \sigma_{2\Delta}$, $\sigma_{1\Sigma} = \sigma_1(\lambda_1)\,\mathrm{sgn}(\lambda_1) + \sigma_1(\lambda_3)\,\mathrm{sgn}(\lambda_3)$, $\sigma_{1\Delta} = \sigma_1(\lambda_1)\,\mathrm{sgn}(\lambda_1) - \sigma_1(\lambda_3)\,\mathrm{sgn}(\lambda_3)$, $\sigma_{2\Sigma} = \sigma_2(\lambda_1) + \sigma_2(\lambda_3)$, $\sigma_{2\Delta} = \sigma_2(\lambda_1) - \sigma_2(\lambda_3)$. The control input variables v_1 and v_2 be $v_1 = \sigma_2(\lambda_1)u_1 - \sigma_2(\lambda_3)u_2$ and $v_2 = \sigma_2(\lambda_1)u_1 + \sigma_2(\lambda_3)u_2$, where $u_1 = \frac{1}{r\omega_1}$ and $u_2 = \frac{1}{r\omega_3}$.

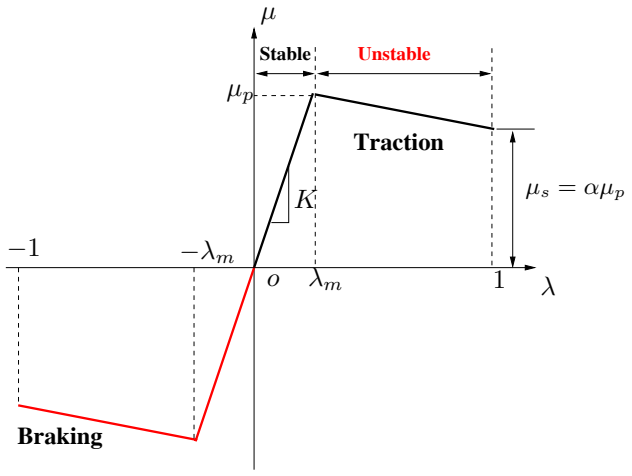

Fig. 3. A linear approximation of the μ-λ relationship.

B. Motion stability

We define the stable motion of the skid-steered mobile robot if the robot is not sliding on the ground surface, namely, the wheel slip satisfies $|\lambda_i| \leq \lambda_m$. The value of S is employed as an indicator for the motion stability. From (3), we take the time derivative and obtain

$$\dot{S}\dot{\psi} + S\ddot{\psi} = -\dot{v}_{Gy}.$$

Substituting robot dynamics (26) into the above equation, we obtain

$$\dot{S}\dot{\psi} = \frac{1}{2}gKv_{Gy}\left[v_2\left(1+\frac{1}{2}\sigma_{r1}\right)+\frac{1}{2}\sigma_{r2}v_1\right] - \frac{mgK}{4I_G}S\left\{-W\sigma_\Delta+\left(Wv_{Gx}+\frac{L^2}{2}\dot{\psi}\sigma_{r1}\right)v_1 - \frac{1}{2}\left[W^2+L^2\left(1+\frac{1}{2}\sigma_{r2}\right)\right]\dot{\psi}v_2\right\}. \quad (27)$$

By the definition of the motion stability, we obtain $\sigma_1 = 0, \sigma_2 = 1, v_1 = \frac{1}{r}\left(\frac{1}{\omega_L}-\frac{1}{\omega_R}\right), v_2 = \frac{1}{r}\left(\frac{1}{\omega_L}+\frac{1}{\omega_R}\right), \sigma_{r1} = 0, \sigma_{r2} = 0, \sigma_\Delta = 0$, and (27) becomes

$$\dot{S} + \frac{gKv_2}{2}\left(a_I - \frac{m}{2I_G}Wy_{Gc}\frac{v_1}{v_2}\right)S = 0, \quad (28)$$

where $a_I = 1+\frac{m}{4I_G}\left(W^2+L^2\right)$.

Without loss of generality, we assume $\omega_L \le \omega_R$ and we have $v_1 \ge 0$, $y_{Gc} > 0$, and

$$\frac{v_1}{v_2} = \frac{\omega_R-\omega_L}{\omega_R-\omega_L} = -\frac{1-\kappa_\omega}{1+\kappa_\omega} \approx -\gamma$$

for small slip values $|\lambda_i| \le \lambda_m$. Using the estimate of S given in (10), we obtain

$$\frac{v_1}{v_2} \approx -\gamma = \frac{a_1}{a_2}\frac{1}{\hat{S}} - \frac{a_3}{a_2}. \quad (29)$$

Substituting (29) into (28) and using the equality $\frac{S}{\hat{S}} = 1+\frac{e_S}{\hat{S}}$, we obtain the dynamics of S as

$$\dot{S} + \zeta_1 S - \sqrt{2}\zeta_2\left(1+\frac{e_S}{\hat{S}}\right) = 0, \quad (30)$$

where $\zeta_1 := \zeta_1(v_2, y_{Gc}) = \frac{gkv_2}{2}\left(a_I + \frac{mWy_{Gc}a_3}{2I_Ga_2}\right)$ and $\zeta_2 := \zeta_2(v_2, y_{Gc}) = \frac{\sqrt{2}gkv_2mWy_{Gc}a_1}{8I_Ga_2}$. Notice that $|\gamma| \le 1$ by definition (9), and from the steady-state value of S, we obtain the condition

$$y_{Gc} = \frac{v_{Gx}}{\dot{\psi}} \ge \frac{2a_II_G}{mW}. \quad (31)$$

Condition (31) implies that for a stable motion of a skid-steered robot, the turning radius has to be larger than the value in the right hand side of (31).

V. Experimental Results

We have built an on-board sensor suite on the skid-steered mobile robot shown in Fig. 1. We use a low-cost IMU from Sentera Technology Inc. The control system is a two-level hierarchy: the control algorithm and the EKF design are located in the on-board laptop system, while the PID-based motor control is located at the low-level real-time system. The on-board real-time system receives the commanded wheel velocity at a frequency of 20 Hz, and the PID-based motor controller is running at a frequency of 1 KHz. The EKF-based localization scheme is updated at a frequency of 125 Hz, which is also the updating frequency of the IMU device. All experiments were conducted at the Texas A&M University campus. We also developed a computer vision-based positioning system to provide the robot's absolute position information in all experiments. The resolution of the vision positioning system is around 1.49 cm. A timing-synchronization mechanism is set up using wireless communication such that we can correspond the on-board localization system with the vision-based positioning system. The output of the computer vision-based localization system thus serves as a ground truth to compare and validate the proposed localization scheme.

We present the experimental results where the skid-steered robot runs on a flat concrete surface. Due to the page limit, we present only results for "8"-shape trajectory. In Fig. 4(a), we show the localization results. For the "8"-shape trajectory, the robot starts with $\omega_L/\omega_R = 80/40$ rpm for about 8 s, and then each side's two wheels simultaneously change their angular velocities by a constant rate of 10 rpm per second until their velocity combination reaches $\omega_L/\omega_R = 40/80$ rpm.

Fig. 4(a) also shows the comparison results of the robot localization under three different schemes. These schemes use three different sets of measurements: (1) both the vertical velocity v_{Bz} constraint (5) and the longitudinal velocity estimate *without* considering the wheel slip; (2) both the vertical velocity constraint and longitudinal velocity estimate *with* the wheel slip feedback (6); and (3) all three-dimensional velocity constraints and estimates incorporating the wheel slip. From Fig. 4(a), we observe that the first scheme has a large error (blue-square line). By considering the wheel slip estimation, the localization results improve significantly (black-triangle line in Fig. 4). Finally, if we consider all three-dimensional velocity constraints and estimations with the slip estimation (blue-dot line), the estimated trajectory is close to the real trajectory.

Fig. 4(b) shows the wheel slip comparisons between the EKF-based estimation and vision-based measurements. In Fig. 4(c), we compare the prediction of EKF velocity estimation errors (blue solid-circle line) with the real errors (red empty-circle line) and they match well. These results validate that the estimated velocity errors are mainly due to the yaw angle estimation error as our analysis. Fig. 5 shows the S-value comparison results for the "8"-shape trajectories. The S values are changing for varying γ values and according to the relationship given in (10).

We also let the robot run on a patch of sand, and thus slide on the ground surface. Fig. 6(a) shows the robot's trajectory. The robot runs under $\omega_L/\omega_R = 80/40$ rpm. The maximum cycle-to-cycle sliding distance on a sandy patch trajectory is around 40 cm, while for a regular trajectory, that distance is only around 20 cm. We clearly observe sliding of the robot platform when it runs on the sandy patch. Fig. 6(b) shows the S values during the robot motion. Three spikes are clearly seen in Fig. 6(b) at times around 2, 10, and 25 s. These spike values are much larger than the typical value (around 10 cm). Therefore, the increases of S values can be used as an indicator for the robot sliding conditions.

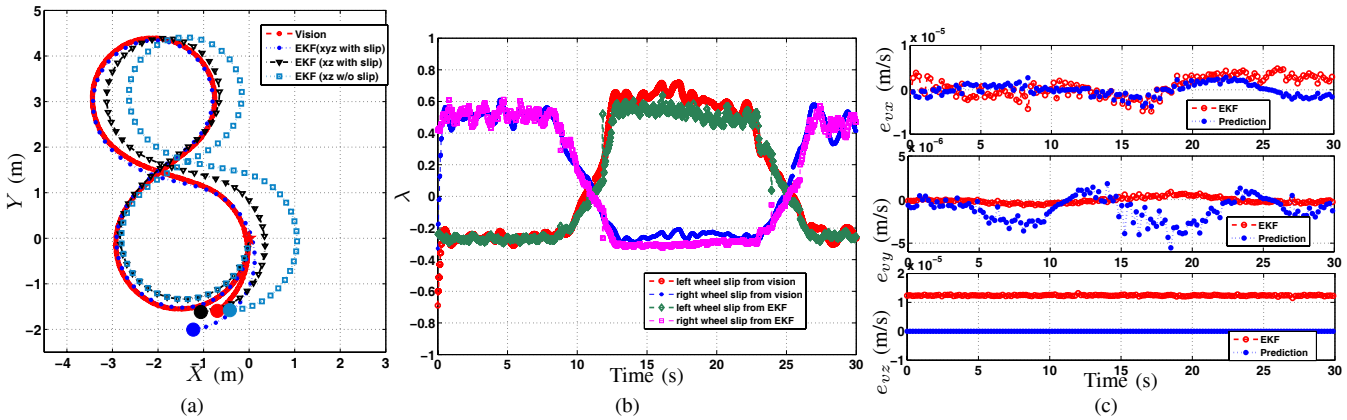

Fig. 4. (a) EKF-based XY trajectory estimation for "8"-shape trajectories. In the figure, the robot starts at the origin (marked as a star symbol) and stops at the symbol marked as a large solid circle. (b) Estimated wheel slip information using EKF-based and computer vision-based localization schemes. (c) EKF-based velocity estimation errors.

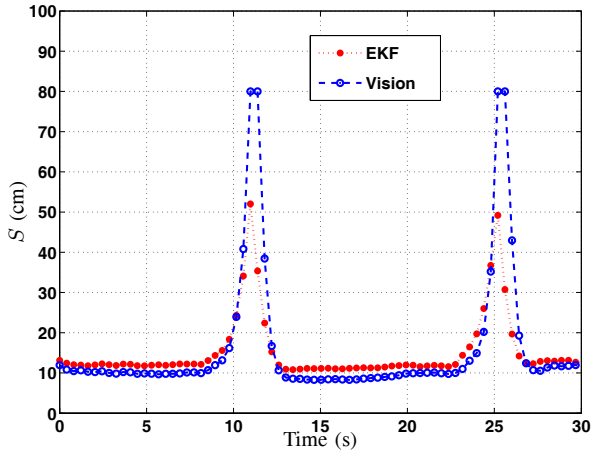

Fig. 5. S-value comparison for the "8"-shape trajectory.

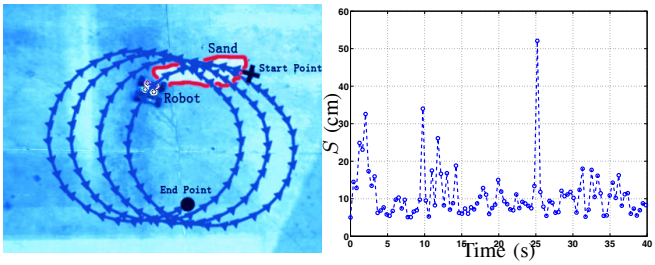

Fig. 6. The skid-steered robot runs a circle trajectory with a sandy patch. (a) Vision-based trajectory with a sandy patch. The robot starting and ending points are marked as a "cross" and a large solid circle symbols, respectively. (b) S curve for the circle trajectory.

VI. Conclusion

Modeling and localization of skid-steered robots are challenging due to the complex robot dynamics and wheel/ground interactions. In this paper, we presented a kinematic and dynamic modeling and analysis of skid-steered mobile robots. The kinematic analysis is based on the motion similarity between the skid-steered robot and tracked vehicles, while the dynamic modeling approach takes advantages of the automotive tire/road interaction models. We presented an EKF-based robot localization scheme that utilized the kinematic modeling and analysis. The analysis and estimation methodology are tested on a robotic testbed with a computer vision-based localization system.

References

[1] J. Yi, J. Zhang, D. Song, and S. Jayasuriya, "IMU-based localization and slip estimation for skid-steered mobile robots," in *Proc. IEEE/RSJ Int. Conf. Intell. Robot. Syst.*, San Diego, CA, 2007, pp. 2845–2850.

[2] J. Yi, D. Song, J. Zhang, and Z. Goodwin, "Adaptive trajectory tracking control of skid-steered mobile robots," in *Proc. IEEE Int. Conf. Robot. Autom.*, Roma, Italy, 2007, pp. 2605–2610.

[3] Z. Song, Y. Zweiri, L. Seneviratne, and K. Althoefer, "Nonlinear observer for slip estimation of skid-steering vehicles," in *Proc. IEEE Int. Conf. Robot. Autom.*, Orlando, FL, 2006, pp. 1499–1504.

[4] A. Le, D. Rye, and H. Durrant-Whyte, "Estimation of track-soil interactions for autonomous tracked vehicles," in *Proc. IEEE Int. Conf. Robot. Autom.*, Albuquerque, NM, 1997, pp. 1388–1393.

[5] G. Anousaki and K. Kyriakopoulos, "A dead-reckoning scheme for skid-steered vehicles in outdoor environments," in *Proc. IEEE Int. Conf. Robot. Autom.*, New Orleans, LA, 2004, pp. 580–585.

[6] J. Martínez, A. Mandow, J. Morales, S. Pedraza, and A. García-Cerezo, "Approximating kinematics for tracked mobile robots," *Int. J. Robot. Res.*, vol. 24, no. 10, pp. 867–878, 2005.

[7] K. Kozlowski and D. Pazderski, "Practical stabilization of a skid-steering mobile robot – A kinematic-based approach," in *Proc. 2006 IEEE Conf. Mechatron.*, Budapest, Hungary, 2006, pp. 519–524.

[8] D. Helmick, S. Roumeliotis, Y. Cheng, D. Clouse, M. Bajracharya, and L. Matthies, "Slip-compensated path following for planetary exploration rovers," *Advanced Robotics*, vol. 20, no. 11, pp. 1257–1280, 2006.

[9] L. Ojeda, D. Cruz, G. Reina, and J. Borenstein, "Current-based slippage detection and odometry correction for mobile robots and planetary rovers," *IEEE Trans. Robotics*, vol. 22, no. 2, pp. 366–378, 2006.

[10] A. Mandow, J. Martínez, J. Morales, J. Blanco, A. García-Cerezo, and J. González, "Experimental kinematics for wheeled skid-steer mobile robots," in *Proc. IEEE/RSJ Int. Conf. Intell. Robot. Syst.*, San Diego, CA, 2007, pp. 1222–1227.

[11] C. Ward and K. Iagnemma, "A dynamic-model-based wheel slip detector for mobile robot on outdoor terrain," *IEEE Trans. Robotics*, vol. 24, no. 4, pp. 821–831, 2008.

[12] G. Dissanayake, S. Sukkarieh, E. Nebot, and H. Durrant-Whyte, "The aiding of a low-cost strapdown inertial measurement unit using vehicle model constraints for land vehicle applications," *IEEE Trans. Robot. Automat.*, vol. 17, no. 5, pp. 731–747, 2001.

[13] K. Weiss, "Skid-Steering," *Auto. Eng.*, pp. 22–25, 1971.

[14] J. Wong and C. Chiang, "A general theory for skid steering of tracked vehicles on firm ground," *Proc. Inst. Mech. Eng., Part D: J. Auto. Eng.*, vol. 215, pp. 343–355, 2001.